

The Detached Eclipsing Binary KV29 and the Age of the Open Cluster M11

Ernest A. Bavarsad¹, Eric L. Sandquist¹, Matthew D. Shetrone², Jerome A. Orosz¹

ABSTRACT

We present an extensive set of photometry and radial velocities for the detached eclipsing binary KV 29 in the intermediate-aged open cluster M11 (NGC 6705). Spectroscopy shows that the system is double-lined and all available evidence (proper motion, photometry, and position on the CMD) indicates it is a member of the cluster. We find the period of the binary to be 4.64276 ± 0.00001 days. We find masses $3.604_{-0.011}^{+0.002} M_{\odot}$ and $1.837_{-0.006}^{+0.001} M_{\odot}$, and radii $5.392_{-0.035}^{+0.018} R_{\odot}$ and $1.656_{-0.044}^{+0.007} R_{\odot}$ for the primary and secondary stars, respectively. Because the primary star in the binary is rapidly evolving and is brighter than the cluster turnoff in a color-magnitude diagram, the measurement of its radius leads to a strong constraint on the cluster age. We find the age of M11 to be $222_{-3}^{+2} \pm 15$ Myr, where the quoted uncertainties come from statistical errors in the calculated masses and radii, and systematic uncertainties due to the ambiguity of the metallicity of the open cluster and variations within the isochrone models concerning heavy elements and convective overshooting.

Subject headings: open clusters and associations: individual (NGC 6705) - stars: evolution - stars: binaries: spectroscopic - stars: binaries: eclipsing - techniques: spectroscopy - techniques: photometry

1. Introduction

One of the most precise ways to determine the ages of stars (besides the Sun) involves the measurement of the masses and radii of evolved stars in detached eclipsing binaries (DEBs). Masses are critical inputs for stellar models that determine the evolutionary timescales, and

¹San Diego State University, Department of Astronomy, San Diego, CA, 92182; eabavarsad@yahoo.com; esandquist@mail.sdsu.edu; jorosz@mail.sdsu.edu

²University of Texas, McDonald Observatory, HC75 Box 1337-L Fort Davis, TX, 79734; shetrone@astro.as.utexas.edu

accurate radii can precisely identify the evolutionary states of the stars. Classical age measurement methods involving the use of isochrones in the color-magnitude (CMD) plane generally have uncertainties (often unstated) of greater than 10% due to continuing difficulties in the precise measurement of distance, reddening, and chemical composition; in theoretical uncertainties in color- T_{eff} relations and stellar interior physics; and due to degeneracies in the effects of each of these things on the isochrones. Fortunately, these issues can largely be avoided using DEB systems where masses and radii can be determined using straightforward physical principles.

Not all DEBs have characteristics that allow precise determinations of age. The most important requirement is that at least one component needs to be starting to rapidly evolve in size — stars that have changed significantly in radius from their zero-age main sequence value break degeneracies involving uncertainties in age, distance, reddening, model physics, and chemical composition (Southworth et al. 2004). Another requirement is that both stars in the DEB must show lines in the spectrum for radial velocity measurements and the eclipses must be strong (preferably total) so that a system inclination can be precisely determined. Lastly, for precise mass and age measurements to be made, the orbital period of the system must not be so short that interactions between the components affect the stars’ characteristics. A star evolving off the main sequence cannot have lost or gained significant mass, as this would critically affect the derived age. More subtly, interactions between the stars can lead to a host of effects from nonsphericity to modified rotation (with its own effects).

M11 is a very rich intermediate-age open cluster, which provides us with a heavily-populated CMD and maximizes our chances of finding useful DEB systems. Hargis et al. (2005) and Koo et al. (2007) surveyed M11 for variable stars, detecting 5 DEBs that potentially meet the criteria for precise age determination. In this paper, we examine the DEB KV29 ($\alpha_{2000} = 18^{\text{h}}51^{\text{m}}00^{\text{s}}.13$, $\delta_{2000} = -6^{\circ}16'37''.4$), identified as an A0 star (Lindblad 1922). McNamara et al. (1977) report that the system has a proper motion cluster membership probability of 98%. Cantat-Gaudin et al. (2014) give it a 0% membership probability based on a radial velocity measurement, but this can be explained by binarity. The photometry of the system ($V = 11.92$; M11-1139 in the tabulation of Stetson 2000) places it brighter than the cluster’s turnoff, meaning that at least one of the stars is likely to be significantly evolved. Koo et al. (2007) showed that the system had eclipses with similar depths ($\Delta V \approx 0.10$ and 0.07 mag), meaning that the system was likely to be double lined. There were signs of modest ellipsoidal variation of about 0.02 mag outside of eclipse, indicating that the stars are slightly nonspherical. This is consistent with the relatively short period of 4.64576 d they reported.

For the purposes of our age analysis below, we will need to have some knowledge of

the cluster metallicity and reddening, although we try to use methods that minimize their importance. In addition, it is worth keeping previous determinations of the cluster age in mind because systematic differences between our eclipsing binary methods and those using CMDs can identify failings in our understanding of the physics governing these stars. Sung et al. (1999) derived $\log(t_{age}) = 8.4 \pm 0.1$ by comparing *UBVI* CMDs with theoretical isochrones, and determined an interstellar reddening $E(B - V) = 0.428 \pm 0.027$ and a distance modulus $(m - M)_0 = 11.55 \pm 0.10$. For the metal content of the stars, Gonzales & Wallerstein (2000) derived a mean $[\text{Fe}/\text{H}]$ value for M11 of 0.10 ± 0.03 by analysing high-quality spectra of 10 bright K giants. As they state, this value of $[\text{Fe}/\text{H}]$ is consistent with the expected value derived from the cluster’s position in the disk (6.9 kpc away from the galactic center) and the trend of increasing metallicity with decreasing distance from the galactic center. Santos et al. (2012) found $[\text{Fe}/\text{H}] = +0.23$ from high-resolution spectroscopy of one giant, although it should be noted that this value involved a metallicity-dependent correction that was extrapolated beyond the $[\text{Fe}/\text{H}]$ values in the original calibrating sample. (The uncorrected value was $+0.13$.) Recently Cantat-Gaudin et al. (2014) found $[\text{Fe}/\text{H}] = +0.10 \pm 0.06$ from spectroscopy of 21 cluster members, and using that composition along with *BVI* and *ri* photometry derived ages between 250 and 316 Myr (depending on the model isochrones used). Beaver et al. (2014) used Strömgren photometry to find the metallicity of M11 to be $[\text{Fe}/\text{H}] = -0.06 \pm 0.05$ from 162 F-type cluster main sequence stars (although there is a large dispersion of 0.59 dex in individual values), and a reddening of $E(B - V) = 0.45 \pm 0.01$ using 332 B-A3 type stars.

2. Observations and Data Reduction

2.1. Photometry

M11 was observed on 37 nights from June 2009 to August 2011 (with one additional night in 2013) in *BVR_C* filters using the 1.0m telescope at Mount Laguna Observatory (hereafter, MLO) with the CCD camera field covering an area approximately $13'5 \times 13'5$, for a scale of about $0'4 \text{ pixel}^{-1}$. The nights of observation are listed in Table 1. Exposure times for varied between 90 and 300 s depending on filter and atmospheric conditions. The exposure time was adjusted throughout the night in order to achieve a peak of about 30,000 counts for the binary system per image. The seeing from our observations generally produced a FWHM of stellar images of 1.5 – 2.5 arcsec. Image processing (overscan subtraction, bias

subtraction, and flat-field correction) was done using standard tools in IRAF¹.

M11 is a heavily-populated open cluster, and crowding in the field is significant. In order to derive precise light curves, we employed point-spread function (PSF) photometry using DAOPHOT and ALLSTAR (Stetson 1987). The PSF was iteratively fit and allowed to vary across the frame according to a quadratic polynomial. Typically around 150 relatively isolated stars were used to determine the PSF.

After photometry was derived for each frame using ALLSTAR, we applied ensemble methods (Honeycutt 1992; Sandquist et al. 2003) to correct the photometric zeropoints for effects such as nightly variations in atmospheric transparency. Because thousands of stars could typically be measured on each image, the zeropoints are very well determined from the stellar ensemble. As the zeropoints are refined, the median instrumental magnitudes for the stars become better determined as well. The median magnitudes and frame zeropoints were iteratively recalculated until all values converged to better than 0.0005 mag.

The depth of the primary eclipses are fairly consistent from filter to filter, but the secondary eclipse is deepest in R_c ($\Delta R_c = 0.07$) as shown in Fig. 1. The radial velocities (see §2.2) show that the cooler, less massive star is behind its companion at the time of secondary eclipse. Figures 2 and 3 show the photometry taken on individual nights of eclipse. Most importantly, the secondary eclipses show evidence of being flat at minimum (see HJDs 2455380, 2455742, and 2455756), suggesting the eclipses are total. This makes it easier to disentangle the amount of light contributed by each star.

The light curves often show variations that may be independent of the eclipses. While spots are not generally expected for stars with radiative envelopes, observations from the *Kepler* mission indicate that they do occur. Balona (2013) found evidence of activity among about 40% of A-type stars. The amplitude of the variations was most commonly in the tens of parts per million, but did occasionally reach mmag levels. Because the primary star is more than 3 mag brighter than the secondary star, an astrophysical source of variability almost certainly originated on the primary. However, longer term monitoring is needed to establish the nature of the variability.

¹IRAF is distributed by the National Optical Astronomy Observatory, which is operated by the Association of Universities for Research in Astronomy, Inc., under cooperative agreement with the National Science Foundation.

2.2. Spectroscopy

Our spectra were obtained at the Hobby-Eberly Telescope (HET) with the High Resolution Spectrograph (HRS; Tull 1998) as part of normal queue-scheduled observing (Shetrone et al. 2007). The configuration of the HRS was chosen based upon the spectral line widths and strength of the secondary in the first spectrum taken of each object. KV29 was observed with a resolution $R = 30000$, a $2''$ fiber feed, and binning to approximately 2.7 pixels per resolution element. The configuration covers 4825 Å to 6750 Å with a small break at 5800 Å between the red and blue CCDs, although we used only the blue section of the spectra. Exposure times were between 480 and 700 s. The data were reduced using the echelle package within IRAF for fairly standard bias and scattered light removal, 1D spectrum extraction, and wavelength calibration.

We obtained a total of 17 spectra between May 2010 and September 2011. In two of these spectra, the lines were heavily blended (to the point that cross correlation peaks were fully blended) and two others had moderate blending. However, based on the width of the lines, the brighter star is clearly rotating more rapidly than the secondary, meaning that the spectral features of the secondary could be marginally identified in the spectra with the heaviest blending.

Our radial velocity measurement procedure made use of broadening functions (Rucinski 1992, 2002) and spectral disentangling (González & Levato 2006). Broadening functions (BFs) transform a sharp-lined spectrum into a broadened spectrum through a convolution, and they contain information on the Doppler shifting of the spectrum as well as broadening effects like rotation. BFs generally improve the measurement of Doppler shifts relative to cross correlation methods in the presence of substantial rotational broadening and overlapping spectral lines, and this is of great importance for a short-period binary like KV 29. We resampled to a common logarithmic wavelength spacing at approximately the same pixel resolution as the original spectra, and employed IDL routines provided publicly by S. Rucinski² to derive the broadening function via singular value decomposition. We used different synthetic spectrum templates with temperatures $T_{\text{eff}} = 10000$ and 8500 K for the two stars, but both having $\log g = 3.557$, and $[\text{Fe}/\text{H}] = +0.10$. We fit the peaks in the BFs with rotational broadening profiles assuming 50 and 20 km s⁻¹, allowing for a modest amount of variation around those values (15 and 4 km s⁻¹, respectively). We found that restricting the analysis to wavelengths between 5000 and 5400 Å produced the clearest broadening functions because this range contained the strongest and best-measured spectral lines.

²<http://www.astro.utoronto.ca/~rucinski/SVDcookbook.html>

To determine precise radial velocities even for the spectra with the most heavily blended lines, we used spectral disentangling. Disentangling involves an iterative procedure of re-determining radial velocities and averaged spectra for each component of the binary repeatedly, with subtraction of the averaged spectrum of one star from each collected spectrum during the measurement of the radial velocities and averaged spectrum (shifted to the rest frame) of the other star. By removing the companion star’s spectrum as best we possibly can, we minimize systematic effects from line blending on the measured radial velocities. The technique works best when there are a sufficient number of spectra taken at different orbital phases with good velocity separation. In our case, we used the 9 spectra with the largest separation in the determination of the average spectra, and the iterations converged rapidly.

We corrected the measured values for heliocentric velocity and spectrograph zero-point offsets. Radial velocity standards were observed on most nights that the binary was, and the difference between the measurement and literature value was used as a zero-point correction for the eclipsing binary measurements. If a standard was not observed on the same night, the correction was determined by averaging measurements from nights nearest in time. From experience, the radial velocity corrections vary only slightly (by a few hundred m s^{-1}) from night to night, but do vary significantly with instrument configuration and season. The final radial velocity values are given in Table 2 and plotted (along with an $O - C$ diagram) in Fig. 4.

By comparing synthetic spectra with the disentangled spectra, we derived constraints on the rotational velocities and temperatures of the two stars. We find temperatures of approximately 10000 and 7500 K, although we will hone our temperature estimates in the next section using photometry. In any case, the spectral types appear to be A0IV and A6V. (Before it reached the turnoff and evolved significantly, the primary probably had a spectral type of B9V.) We find rotation speeds of 46 and 18 km s^{-1} with uncertainties of approximately 4 and 2 km s^{-1} , respectively. Based on these speeds and later determination of the stellar radii, both stars appear to be rotating approximately in synchronism with the orbit. This is somewhat surprising given that the primary star probably expanded by about a factor of two in the last 40 Myr as a result of its evolution. The rotation of the primary may be lagging behind synchronism slightly — further analysis of this system could place interesting constraints on tidal effects on the rotation.

3. Binary Star Modeling

In order to model the photometric and spectroscopic data of KV29, we used the ELC code (Orosz & Hauschildt 2000), which employs a Markov chain Monte Carlo (Tegmark et

al. 2004) algorithm to optimize the fit. Because the spectroscopic results indicate the binary orbit has zero eccentricity, some orbit parameters (namely the velocity semi-amplitude of the primary star K_p , and the ratio of the stellar masses $Q = M_2/M_1$) can be determined from spectroscopic velocities independent of the light curves. We therefore fitted the radial velocities first, searching for the minimum χ^2 , while also examining models with alternate parameter sets in order to evaluate uncertainties. The uncertainties in the binary model parameters were derived from the range of parameter values that produce a total χ^2 within 1 of the minimum value, which approximates a 1σ uncertainty (Avni 1976). Because the velocity measurement uncertainties are used in the calculation of χ^2 , it is important that these uncertainties be as realistic as possible. Usually measurement uncertainties calculated during the data reduction process are underestimated, which would inflate the total χ^2 value and lead to an underestimation of the uncertainties in the binary star model parameters. With awareness of this, we scaled the uncertainty estimates of the radial velocities from the spectroscopic analysis (and later, the photometric measurements in each filter) upward to return a reduced χ^2 value of 1 for each measured quantity in order to be consistent with the observed scatter around the best fit model. The results for K_p and Q are tabulated in Table 3.

We then proceeded to light curve fitting. Because the degree of limb darkening has a significant effect on measured radii for systems like KV29 having shallow eclipses, we probed the potential systematic errors by fitting with different limb darkening descriptions. We first used a quadratic limb darkening law with coefficients taken from Claret & Bloemen (2011) and using PHOENIX model atmospheres (Hauschildt et al. 1997) to normalize the brightness from the centers of the visible star disks. The parameters we fit for were orbital period P , time of conjunction (primary eclipse) t_o , inclination i , ratio of the stellar radii to average orbital separation R_1/a and R_2/a , and temperature ratio T_2/T_1 . K_p , Q , and T_1 were held as external constraints. These observational constraints impose a χ^2 penalty on models if the parameter values deviate from values determined earlier. The $\chi^2 - \chi_{min}^2$ plot for the 6 parameters P , T_o , i , R_1/a , R_2/a , and T_2/T_1 in this run (constant limb darkening coefficients) can be seen in Fig. 5. A model fit of the eclipses can be seen in Fig. 6.

We also conducted fits while allowing the limb darkening coefficients to vary, following the algorithm of Kipping (2013). Due to the scatter in the observed light curves, we examined the effects of using weighted average photometry for phase bins. (See Schiller & Milone 1988 for a similar usage for the short-period eclipsing binary DS Andromedae.) We used phase bins of 0.002 in and near eclipses (0.90 to 0.10 and 0.40 to 0.60) and 0.01 elsewhere. The uncertainty of each binned point was taken to be the error of the weighted mean. Results from both runs can be seen in Table 4, and some fitted quantities can be seen to deviate by several standard deviations (T_{rat}). The difference in the lightcurve shapes from filter to

filter has made it difficult to fit for limb darkening coefficients, but the fitted parameters for the binned run mostly agree with those of the full data run. Although there are changes to the measured stellar radii depending on the method of fitting, it should be noted that these small differences negligibly affect our age determination in the next section because the primary star is in a phase of rapid radius evolution. The masses are more important for the age determination here, and the quantities $a \sin i$, $M_1 \sin^3 i$, $M_2 \sin^3 i$ from each model agree to less than 1σ .

Ellipsoidal variations are visible in the out-of-eclipse observations plotted in Fig. 1, suggesting that at least one of the stars is tidally distorted, in agreement with the expectations for the short orbital period and evolved state of the primary star. The ELC code uses a Roche lobe geometry to model the non-spherical nature of the stars in the binary and its effects on the light curve. The Roche lobe filling factor for the primary star was calculated to be 0.470, much larger than that of the secondary at 0.176. Because the primary star is much brighter than the secondary star, almost all of the out-of-eclipse variation in the lightcurves is caused by the primary.

As mentioned before, we see that during the secondary eclipse the primary star is totally blocking the light of its companion. Because the primary star alone is visible then, the secondary eclipse depths allow us to disentangle the photometry of the two stars. We did this with two different methods. First, we carefully measured the secondary eclipse depths and used them to infer the brightness of the primary star. The following nights (in HJD) were used: 2455394, 2455401, 2455410, 2455417, 2455424, and 2455763 in B , and 2455011, 2455380, 2455387, 2455410, 2455417, and 2455424 in V . We took the average of the out-of-eclipse observations for a given night and subtracted it from the average of the points during totality. We found eclipse depths $\Delta B = 0.055 \pm 0.002$ and $\Delta V = 0.066 \pm 0.002$. For stars with significant non-sphericity, the depths only provide upper limits to the luminosity ratio because we are looking down the long axis of an elongated star during the eclipses. We therefore derived luminosity ratios from ELC model fits to all of the light curve data (see Fig. 6). We found the $\chi^2 - \chi_{min}^2$ for the luminosity ratios L_2/L_1 for each color in the fitted limb darkening run (Fig. 7) and used those to decompose the photometry of the stars. The ELC models yielded $L_{B2}/L_{B1} = 0.040 \pm 0.001$, $L_{V2}/L_{V1} = 0.050 \pm 0.001$, and $L_{R2}/L_{R1} = 0.059 \pm 0.001$, where the quoted uncertainties are statistical. We have chosen to include a contribution to the uncertainty of 0.002 from systematic error resulting from variations in eclipse depths. The decomposed photometry for the two stars can be seen in Table 5.

Using the decomposed $B - V$ colors for both stars, we calculated photometric T_{eff} values using the transformation equations of Casagrande et al. (2010). For that purpose, we used

a cluster reddening $E(B - V) = 0.43$ (Sung et al. 1999) and metallicity $[\text{Fe}/\text{H}] = +0.10$ (Gonzales & Wallerstein 2000). By this method, T_1 was found to be 9480 ± 550 K and $T_2 = 7810 \pm 480$ K. This value for T_2 is roughly consistent with what can be derived from the value of T_1 and the temperature ratio derived from the fitted limb darkening run ($T_2 \approx 8100$ K). Uncertainties in the effective temperatures come from uncertainty in the reddening and metallicity, and in the temperature ratio provided by ELC. Abundance uncertainties (such as the difference between the Gonzales & Wallerstein spectroscopic results and the Beaver et al. (2014) determination of $[\text{Fe}/\text{H}] = -0.06$ using Strömgren photometry) have negligible effects (~ 10 K) on this calculation.

4. Discussion and Analysis

The radii of evolved stars can make excellent age indicators because they can be measured to high precision in eclipsing binary systems and their use avoids systematic errors that are commonly present in other indicators. However, the translation from stellar radius to age requires the use of theoretical mass-radius isochrones. Every isochrone set employs an assumed value for the heavy element content of the Sun (Z_\odot) because it is not a directly measured quantity. Because the metallicity ($[\text{Fe}/\text{H}]$, and therefore Z) of other stars is judged relative to the Sun, this has a potentially significant effect on the age determination if the Sun’s metal content is systematically different from what is assumed. After a thorough re-examination of the solar abundance mix, Asplund et al. (2009) found $Z_\odot = 0.0134$, which is lower than most values assumed in models. If the Asplund et al. value is correct, we should select the heavy element abundance Z of the models based on the revised Z_\odot . Using this new value of Z_\odot and the Gonzales & Wallerstein (2000) spectroscopic $[\text{Fe}/\text{H}]$ value, the M11 metal content should be $Z = 0.0161$. While the PARSEC models allow direct input of a particular Z value, we had to choose Z values as close as possible to that of M11 for the Victoria-Regina and BaSTI isochrone models. The PARSEC isochrones (Bressan et al. 2012) will be used as our primary theoretical isochrone set, with the Victoria-Regina (VandenBerg et al. 2006) and BaSTI (Pietrinferni et al. 2004) models as comparisons.

Fig. 8 contains comparisons with mass versus radius ($M - R$) isochrones. The uncertainty in KV29B’s radius encompasses all four isochrones depicted at its measured mass — it is not sensitive to age because it has not changed significantly in radius since the zero-age main sequence. While the fractional uncertainty in the radius for KV29A is larger than that of the mass (0.6% versus 0.3%), the uncertainty in the derived age is rather small because stellar radii increase quite rapidly near the turnoff, so that mass becomes the more important quantity for determining age. Using the mass and radius of KV29A, the PARSEC

isochrones return an age for M11 of $222_{-3}^{+2} \pm 5$ Myr. The first set of quoted uncertainties are from the statistical measurement uncertainties for the mass and radius, but systematic errors are currently a larger contributor to the age uncertainty at present. As discussed earlier, Beaver et al. (2014) determined a lower metallicity for M11 ($[\text{Fe}/\text{H}] = -0.06 \pm 0.05$) using Strömgren photometry, and their $[\text{Fe}/\text{H}]$ along with the Asplund et al. solar abundance implies $Z = 0.0117 \pm 0.0015$. The lower metallicity PARSEC models yield a younger age of 221 Myr, and this is the basis of the quoted ± 5 Myr uncertainty. The $M - R$ comparisons for lower metallicity isochrones in the PARSEC and Victoria-Regina sets are shown in Fig. 9. For the Victoria-Regina isochrones in Fig. 9, we displayed tracks for $Z = 0.0120$ only, as it is very close to the target value of $Z = 0.0117$. The preferred Z still lies in the range chosen for the BaSTI model of Fig. 8, and shows a younger age near 215 Myr by the same method. We note that a higher Z value (possibly because the Asplund et al. 2009 value for Z_{\odot} is underestimated) would improve the agreement between the models and the $M - R$ combination for the secondary star and would increase the measured age.

Differences in the physics incorporated in different sets of model isochrones can also produce age uncertainties, and we estimate the size of these uncertainties by examining Victoria-Regina and BaSTI isochrones. Interpolating between the Victoria-Regina isochrones with $Z = 0.0146$ and $Z = 0.0170$, we find an age near 235 Myr. Interpolating between BaSTI models with $Z = 0.01$ and $Z = 0.0198$, we find an age near 215 Myr. Based on these factors, we estimate a systematic error due to model physics of approximately ± 10 Myr.

Previous work on M11 has derived ages between 250 and 320 Myr — almost a 30% range in ages. Our preferred age is approximately 9% lower than previously determined by Sung et al. (1999) but marginally consistent. The measurement uncertainty in the age is less than 4%, but it must be remembered that this is model dependent and rests on the validity of the chemical composition and physics used in the stellar models. One of the most important physics issues is convective core overshooting because it critically affects the amount of hydrogen that is burned during the main sequence phase — more overshooting brings more fuel into the core, delays core hydrogen exhaustion, and produces younger looking stars. BaSTI isochrones employ a larger amount of convective core overshooting than the other models (which affects core hydrogen exhaustion and the “kink” at the cluster turnoff in the isochrones in the CMD).

The primary reason there has been such a large amount of disagreement among earlier age studies is that there is little reason to prefer an age based on isochrone shape alone. With a combination of the masses and photometry we bring to bear here, it is unnecessary to fit isochrone shape. In Section 3.2, we derived the photometry for the two stars using the BV photometry for KV29 and luminosity ratios for each filter band from the binary star

models. In Fig. 10, we plot each component on a CMD. The photometry for the CMDs was taken from Stetson (2000), and the stars chosen for the CMD are high probability members of M11 based on proper motions from McNamara et al. (1977). Each isochrone was shifted to match the secondary star’s mass and photometry simultaneously. The secondary star is an unevolved main sequence star, and its position should be relatively insensitive to physics in the stellar models. The primary star’s mass and photometry then constrain the cluster’s age, as do the CMD positions of upper main sequence stars. In Fig. 10, the predicted position of the primary star (given its measured mass) is marked as a circle matching the color of the isochrone for each age. (For some ages, a star with the primary’s mass would have already evolved off the main sequence, and is not visible in the figure.) Roughly speaking, each isochrone set predicts a CMD position for the primary star that is in rough agreement with what is expected from the $M - R$ diagrams discussed above.

For young clusters like M11, the lack of subgiant stars makes it difficult to precisely identify where the turnoff lies. None of the isochrone sets does a particularly good job of matching the characteristics of the upper main sequence, although an unidentified population of unresolved binaries there could be influencing that comparison. Binary stars on the main sequence obscure where single stars terminate in the CMD: the combined light of a brighter MS star at the turnoff with a fainter companion can displace an unresolved binary vertically in the CMD. The theoretical models all predict that there is a large acceleration in the rate of radius change at the cluster turnoff where there is a small kink in the CMD. However, there are seemingly main sequence stars brighter than this point in the CMD, as can be seen in Fig. 10. Based on the expectations for a rapid decrease in the evolutionary timescale after central hydrogen exhaustion and the observed lack of stars on the subgiant branch, there should be few or no stars on the main sequence brighter than this kink. This leads to the prediction that the stars brighter than KV29A will be found to be either blue stragglers or unidentified binaries after more detailed examination. The fact that the brightest of the main sequence stars is a little more than 0.75 mag brighter than KV29A provides some additional evidence that KV29A may be a star that is very close to central hydrogen exhaustion.

On a final note, the giant clump tends to be too bright in the PARSEC models compared to the observations. However, this is not necessarily a way of distinguishing between metallicities because of the effects that different physics (like convective mixing length) and color-temperature transformations can have.

There are several ways in which the isochrone comparisons can be improved with future work. Along with KV29, Koo et al. (2007) found two other detached binary candidates near the turnoff (KV35 and KV36), and there may be others. Characterization of systems like these will improve the precision of the age comparison and can also provide constraints

on chemical composition variables like the difficult-to-measure helium abundance (Brogaard et al. 2011). Both systems are more challenging to analyze fully: KV35 has strong spot modulation in its light curve, and KV36 has a period very near 12 sidereal days. We currently have both systems under study, but new discoveries would help more clearly establish the cluster age by allowing us to check the fidelity of the isochrones and the physics that goes into them. In addition, radial velocity information on the brightest cluster members (e.g. Mathieu et al. 1986) would help clean the CMD of unresolved binaries that conceal the position of the cluster evolutionary sequence, especially at the bright end of the main sequence and subgiant branch. Cantat-Gaudin et al. (2014) presented radial velocities for a large sample of cluster stars, and find several stars brighter than KV29 that are radial velocity members, although these were not monitored for a long enough period to be certain that they are single. Stars that could be validated as single cluster members would produce a significant constraint on the age. Although there are cluster members with colors between the main sequence and red clump, the evidence so far is that these are binary stars. Two stars with $V \approx 11.4$ and $1.0 \lesssim B - V \lesssim 1.2$ (identifiers MPS 926 and 1223 in McNamara et al. 1977) are single-lined spectroscopic binaries that each probably contain a giant and a main sequence star, while another (MPS 1364) has a velocity that is slightly offset from the cluster mean, possibly indicating binarity (Lee et al. 1989). We identified one other likely cluster member (MPS 670) that is closer to, but redder than, the main sequence and should be studied to identify whether it is a binary or a subgiant.

As a final task, we can calculate a luminosity for each star in KV29 using the photometric effective temperatures and radii from the binary analysis. With $R_1 = 5.39_{-0.04}^{+0.02} R_\odot$ and $T_{\text{eff},1} = 9480 \pm 550$ K, the primary star has a luminosity of $212 \pm 49 L_\odot$. The secondary star, with $R_2 = 1.66_{-0.04}^{+0.01} R_\odot$ and $T_{\text{eff},2} = 7810 \pm 480$ K, has a luminosity of $9.2 \pm 2.3 L_\odot$. Using a bolometric correction ($BC = -0.13$; Flower 1996) along with R and T_{eff} , we can compute the distance modulus $(m - M)_V$. We find $M_{V1} = -0.93$ and $(m - M)_V = 12.90 \pm 0.25$ from the primary star. Distance modulus calculations using the secondary star ($BC = 0.03$; Flower 1996) give $(m - M)_V = 12.91 \pm 0.27$. In both cases, the uncertainty is dominated by the temperature uncertainty, but we have included contributions from the radius and bolometric corrections (probably at the level of a few centimag: for example, values from Vandenberg & Clem (2003) are -0.15 and 0.02 for the two stars). So, the binary star measurements are very consistent with each other, giving a weighted average of $(m - M)_V = 12.91 \pm 0.18$. This is consistent with the dereddened distance modulus given by Sung et al. (1999) of $(m - M)_0 = 11.55 \pm 0.10$ if we use their reddening and a traditional extinction factor $R_V = A_V/E(B - V) = 3.1$.

5. Conclusion

We have presented a study of the characteristics of the stars in the eclipsing binary KV29 that is a member of the open cluster M11 and is found at the cluster turnoff. The DEB follows a nearly circular orbit with a period of 4.6428 d, and it shows a total eclipse of the secondary star. The primary star is significantly evolved, possessing a radius that is significantly larger than a main sequence star of the same mass, which puts the star at the turnoff of the CMD for the cluster. We have derived an age of $222_{-3}^{+2} \pm 15$ Myr for M11 using isochrone models with the most up-to-date physics inputs with uncertainties stemming from errors in the calculated masses and radii, and the systematic uncertainties from the metallicity of the open cluster and differences in the physics used in different isochrone models. We have also determined a distance modulus $(m - M)_V = 12.91 \pm 0.18$, incorporating uncertainties in the extinction, metallicity, and temperature.

The stars in the binary appear to be rotating close to synchronism, despite the relatively rapid radius evolution of the primary about over the last ~ 40 Myr. The binary appears to have fairly strong tidal interactions now, and is clearly destined for strong interactions in the near future. Models indicate that the primary star will expand up to $6 - 6.5R_{\odot}$ over the next 15 Myr. After a short contraction back to near its present size, it will rapidly expand and overflow its Roche lobe shortly after beginning to transit the Hertzsprung gap on a thermal timescale. Strong mass transfer will be aided by shrinkage of the orbital separation and of the primary’s Roche lobe, and will make it impossible for the lower-mass secondary star to accommodate the donated gas, leading to a contact phase. After the system’s mass ratio has been reversed, the current primary star will eventually complete its mass transfer, and the system will be fairly quiescent until the current secondary star evolves and expands and starts an Algol mass-transfer phase in the system.

The *BVR* light curves for KV29 showed significant amounts of variation, making it challenging to precisely determine the radii of the two components. We binned the lightcurves in phase in order to smooth these variations. We find uncertainties in the primary and secondary radii of 0.6% and 2.7%, respectively. In spite of these errors, the age uncertainty is rather low due to the evolved nature of the primary star. The age of the primary is very sensitive to the value of its mass (Southworth et al. 2004), and as a result we have improved the precision of the cluster age over CMD-based methods that are subject to more substantial systematic errors related to interstellar extinction. Our age determination is lower than all previous CMD-based determinations, and has considerably higher precision.

With the precision of M11’s age, it can be put confidently in perspective relative to other clusters, and this allows calibration of other age indicators. Stellar rotation (Barnes 2007) is an important age indicator because it can potentially be applied to individual field

stars and it retains sensitivity to age on the main sequence when many other characteristics of stars are changing minimally. The primary limitation of gyrochronology is the need for calibrators of known age, and open clusters like M11 provide that. When the calibrating clusters have precisely known ages, there is no ambiguity as to the relative ages of different clusters. With an age uncertainty of a few percent, the rotation periods measured for M11 stars (Messina et al. 2010) as a function of mass (or rather, its proxy, color) can be reliably compared with clusters of similar age like M35 (Meibom et al. 2009), M34 (Meibom et al. 2011), and M37 (Messina et al. 2008).

The photometry of the secondary star in the eclipsing binary appears to put it in the instability strip where it crosses the main sequence. This part of the instability strip is inhabited by δ Scuti and γ Doradus pulsating stars, and more than a dozen δ Sct stars have previously been detected via their photometric variability (Hargis et al. 2005; Koo et al. 2007; Lee et al. 2010). Seven δ Sct are likely cluster members according to proper motions (McNamara et al. 1977), but these are likely to be just the stars with the highest pulsation amplitudes. With higher precision photometry, the pulsation characteristics of the stars in this cluster ensemble may enable an independent determination of the cluster distance modulus. The measured mass of the secondary star could also help directly constrain the properties of the pulsators in M11 and produce stronger tests of how well we understand their pulsation spectra.

The measurement precision on the characteristics of KV29 will improve with additional spectroscopic and photometric eclipse observations that allow us to reduce the influence of the observed variability in the light curve shape. Improved determination of the effective temperatures would improve the distance modulus and the spectral typing of both components, and would have some effect on the eclipse modelling through the limb darkening prescription. Photometric data in additional colors (like I band) and improved spectroscopic constraints would improve this. As mentioned before, we are in the process of investigating other DEBs in M11 that are known to display eclipses. With the high-precision study of multiple eclipsing systems in the cluster, we will be able to statistically hone the cluster age.

This work has been funded through grant AST 09-08536 from the National Science Foundation to E.L.S. We would like to thank the Director of Mount Laguna Observatory (P. Etzel) for generous allocations of observing time, and K. Brogaard for the use of his spectral disentangling code.

The Hobby-Eberly Telescope (HET) is a joint project of the University of Texas at Austin, the Pennsylvania State University, Stanford University, Ludwig-Maximilians-Universitat Munchen, and Georg-August-Universitat Gottingen. The HET is named in honor of its prin-

cial benefactors, William P. Hobby and Robert E. Eberly.

This research made use of the SIMBAD database, operated at CDS, Strasbourg, France; the NASA/IPAC Infrared Science Archive, which is operated by the Jet Propulsion Laboratory, California Institute of Technology, under contract with the National Aeronautics and Space Administration; and the WEBDA database, operated at the Institute for Astronomy of the University of Vienna.

REFERENCES

- Alard, C. 2000, *A&AS*, 144, 363
- Asplund, M., Grevesse, N., Sauval, A.J., Scott, P. 2009, *ARA&A*, 47, 481
- Avni, Y. 1976, *ApJ*, 210, 642
- Balona, L. A. 2013, *MNRAS*, 431, 2240
- Barnes, S. A. 2007, *ApJ*, 669, 1167
- Beaver, J., Kaltcheva N., Briley M., & Piehl D. 2014, *PASP*, 125, 934
- Bressan, A., Marigo, P., Girardi, L., Salasnich, B., Dal Cero, C., Rubele, S., & Nanni, A. 2012, *MNRAS*, 427, 127
- Brogaard, K., Bruntt, H., Grundahl, F., et al. 2011, *A&A*, 525, A2
- Cantat-Gaudin, T., Vallenari, A., Zaggia, S., et al. 2014, *A&A*, 569, A17
- Casagrande, L., Ramirez, I., Melendez, J., Bessell, M., & Asplund, M., 2010, *A&A*, 512, A54
- Charbonneau, P. 1995, *ApJS*, 101, 309
- Claret, A. & Bloemen, S. 2011, *A&A*, 529, 75
- Flower, P.J. 1996, *ApJ*, 469, 355
- Gonzales, G. & Wallerstein, G., 2000, *PASP*, 112, 1081
- González, J. F., & Levato, H. 2006, *A&A*, 448, 283
- Hargis, J. R., Sandquist, E. L., & Bradstreet, D. H. 2005, *AJ*, 130, 2824 (HSB05)
- Hartman, J. D., Bakos, G., Stanek, K. Z., & Noyes, R. W. 2004, *AJ*, 128, 1761

- Hauschildt, P. H., Baron, E., & Allard, F. 1997, *ApJ*, 483, 390
- Hinkel, K., Wallace, L., Harmer, D., Ayres, T., & Valenti, J. 2000, *IAU Meeting 24, Joint Discussion 1, Atomic and Molecular Data for Astrophysics: New Developments, Case Studies, and Future Needs*
- Honeycutt, R. K. 1992, *PASP*, 104, 435
- Kipping, D. M. 2013, *MNRAS*, 435, 2152
- Koo, J.R., Kim, S.L., Rey, S.C., Lee, C.U., Kim, Y.H., Kang, Y.B., & Jeon, Y.B., 2007, *MNRAS*, 119, 1233
- Lee, C.-U., Koo, J.-R., Kim, S.-L., et al. 2010, *Journal of Astronomy and Space Sciences*, 27, 289
- Lee, C. W., Mathieu, R. D., & Latham, D. W. 1989, *AJ*, 97, 1710
- Lindblad, B. 1922, *ApJ*, 55, 85
- Mathieu, R. D., Latham, D. W., Griffin, R. F., & Gunn, J. E. 1986, *AJ*, 92, 1100
- McNamara, B. J., Pratt, N. M., & Sanders, W. L. 1977, *A&AS*, 27, 117
- Meibom, S., Mathieu, R. D., & Stassun, K. G. 2009, *ApJ*, 695, 679
- Meibom, S., Mathieu, R. D., Stassun, K. G., Liebesny, P., & Saar, S. H. 2011, *ApJ*, 733, 115
- Messina, S., Distefano, E., Parihar, P., et al. 2008, *A&A*, 483, 253
- Messina, S., Parihar, P., Koo, J.-R., et al. 2010, *A&A*, 513, A29
- Metcalfe, T. S. 1999, *AJ*, 117, 2503
- Orosz, J.A. & Hauschildt, P.H. 2000, *A&A*, 364, 265
- Orosz, J. A., Groot, P. J., van der Klis, M., et al. 2002, *ApJ*, 568, 845
- Pietrinferni, A., Cassisi, S., Salaris, M., & Castelli, F. 2004, *AJ*, 612, 168
- Rucinski, S. M. 1992, *AJ*, 104, 1968
- Rucinski, S. M. 2002, *AJ*, 124, 1746
- Sandquist, E. L., Latham, D. W., Shetrone, M. D., & Milone, A. A. E. 2003, *AJ*, 125, 810

- Santos, N. C., Lovis, C., Melendez, J., et al. 2012, *A&A*, 538, A151
- Shetrone, M., et al. 2007, *PASP*, 119, 556
- Schiller S.J. & Milone E.F., 1988, *AJ*, 95, 5
- Southworth, J., Zucker, S., Maxted, P.F.L., & Smalley, B., 2004, *MNRAS*, 355, 986
- Stetson, P. B. 1987, *PASP*, 99, 191
- Stetson, P. B, 2000, *PASP*, 112, 925
- Sung, H., Bessell, M.S., Lee, H.W., Kang, Y.H., & Lee, S.W., 1999, *MNRAS*, 310, 982
- Tegmark, M., Strauss, M. A., Blanton, M. R., et al. 2004, *Phys. Rev. D*, 69, 103501
- Tull, R.G. 1998, *Proc. SPIE*, 3355, 387
- Uytterhoeven, K., Moya, A., Grigahcène, A., et al. 2011, *A&A*, 534, A125
- Van Hamme, W. 1993, *AJ*, 106, 2096
- VandenBerg, D. A., Bergbusch, P. A., & Dowler, P. D. 2006, *ApJS*, 162, 375
- VandenBerg, D. A., & Clem, J. L. 2003, *AJ*, 126, 778
- Wilson, R.E. 1990, *ApJ*, 356, 613

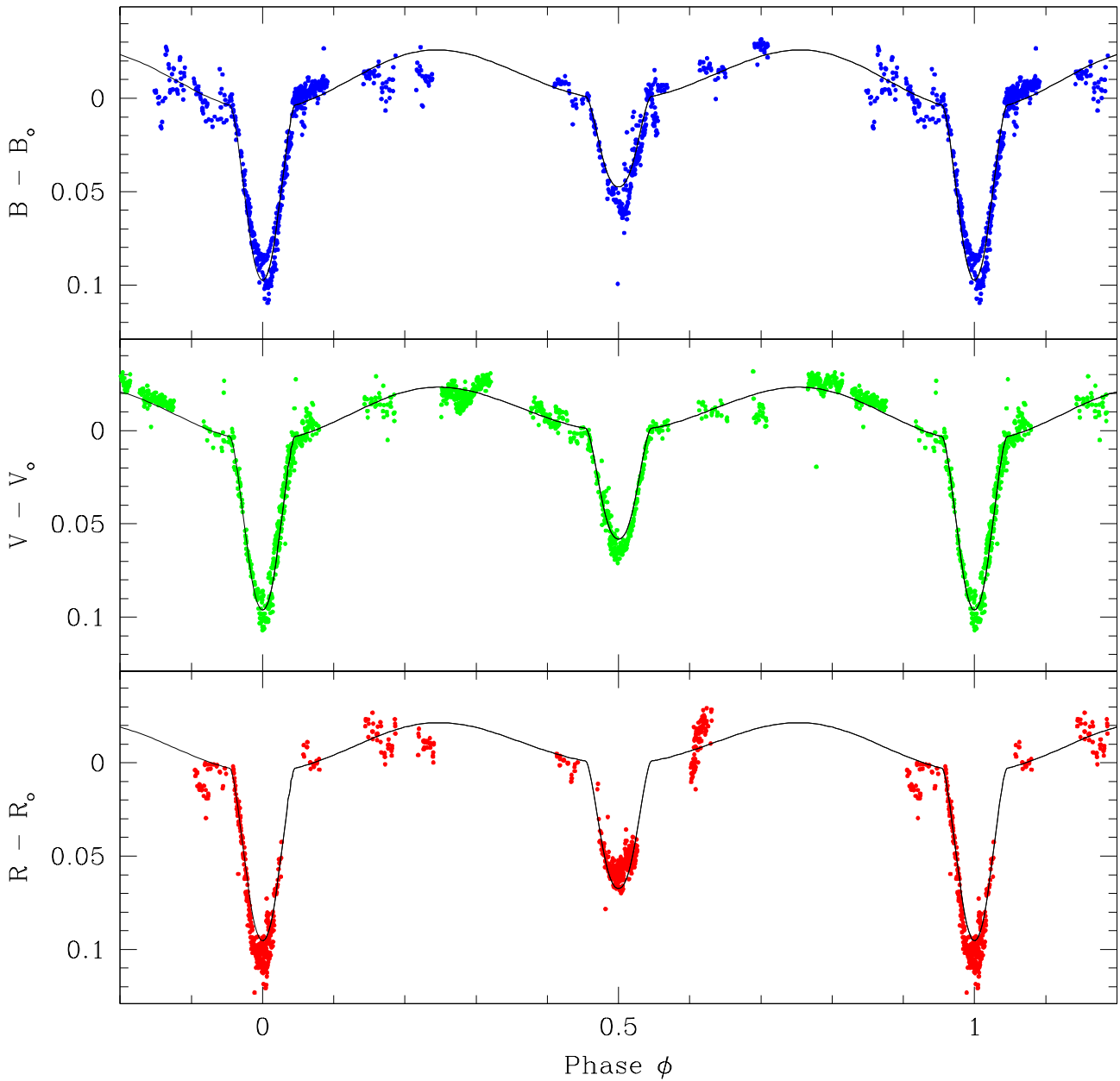


Fig. 1.— Phase-folded light curves for KV29 in B (*top panel*), V (*middle panel*), and R_C (*bottom panel*), referenced to the median magnitude in each filter. The model fit (black line) is from the full data run with fixed limb darkening coefficients.

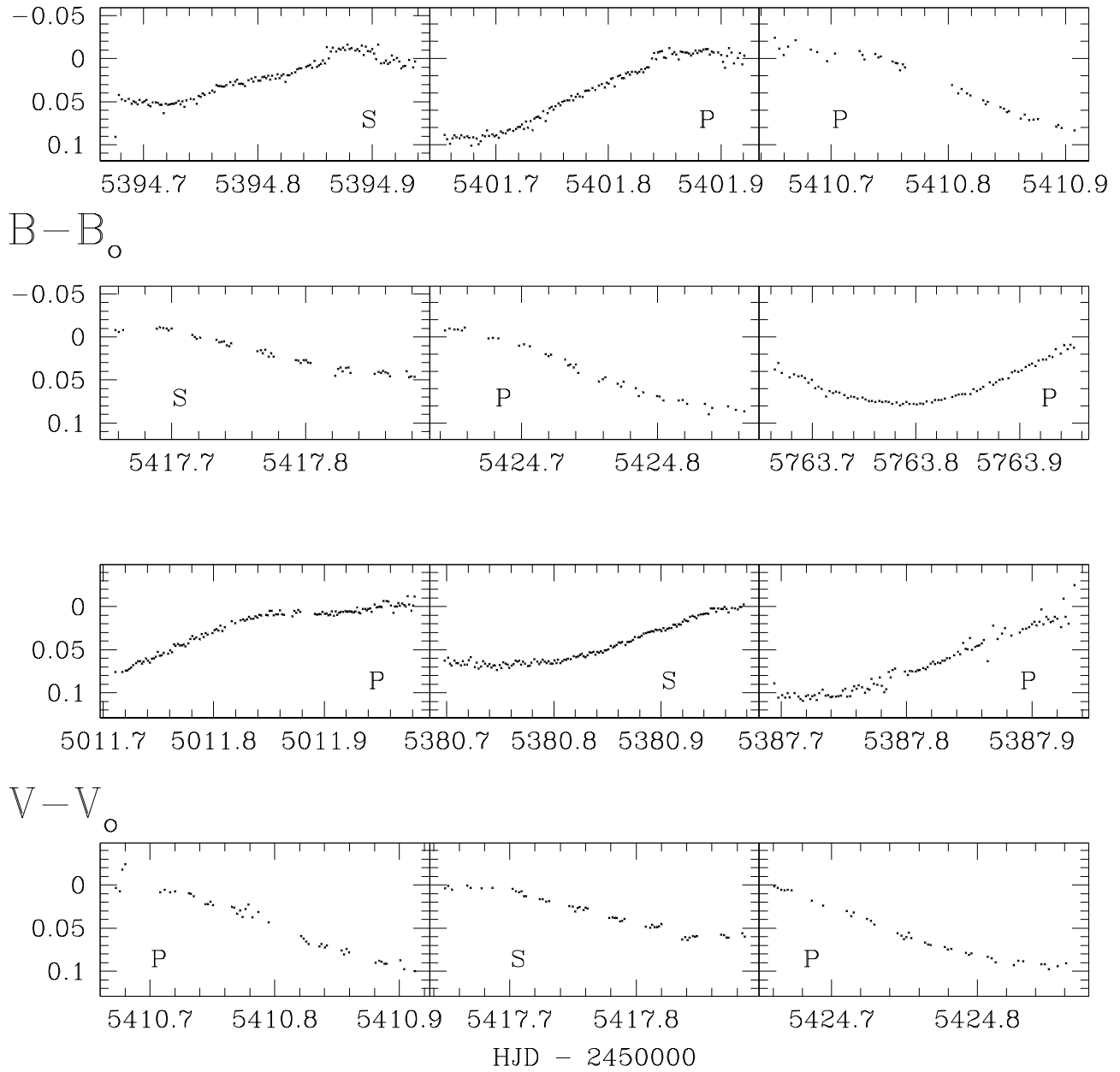


Fig. 2.— MLO photometry of all eclipse nights in BV filters, referenced to the median magnitude. Graphs are labeled “P” and “S” for primary and secondary eclipses, respectively.

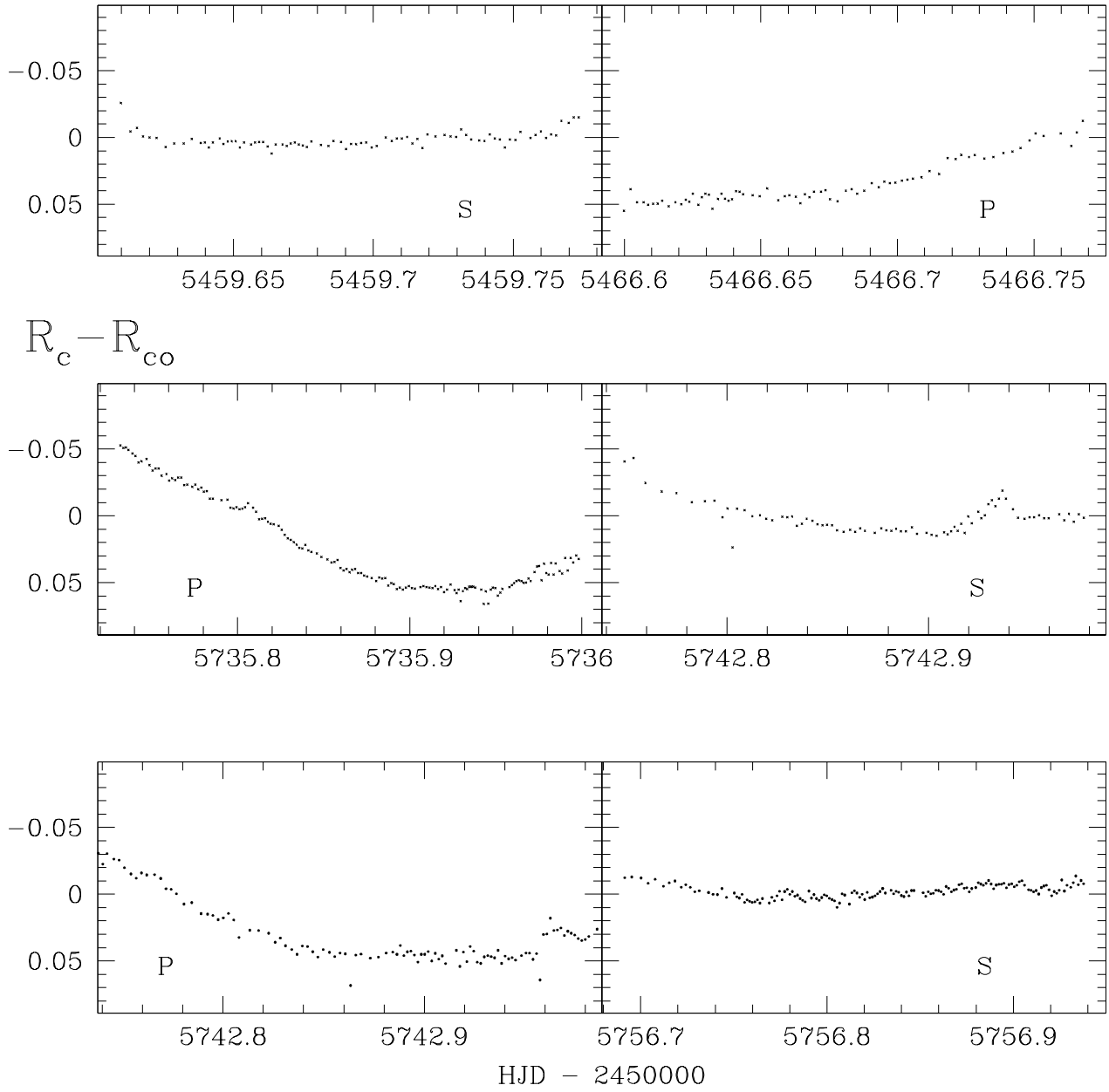


Fig. 3.— MLO photometry of all eclipse nights in R_c , referenced to the median magnitude. Graphs are labeled “P” and “S” for primary and secondary eclipses.

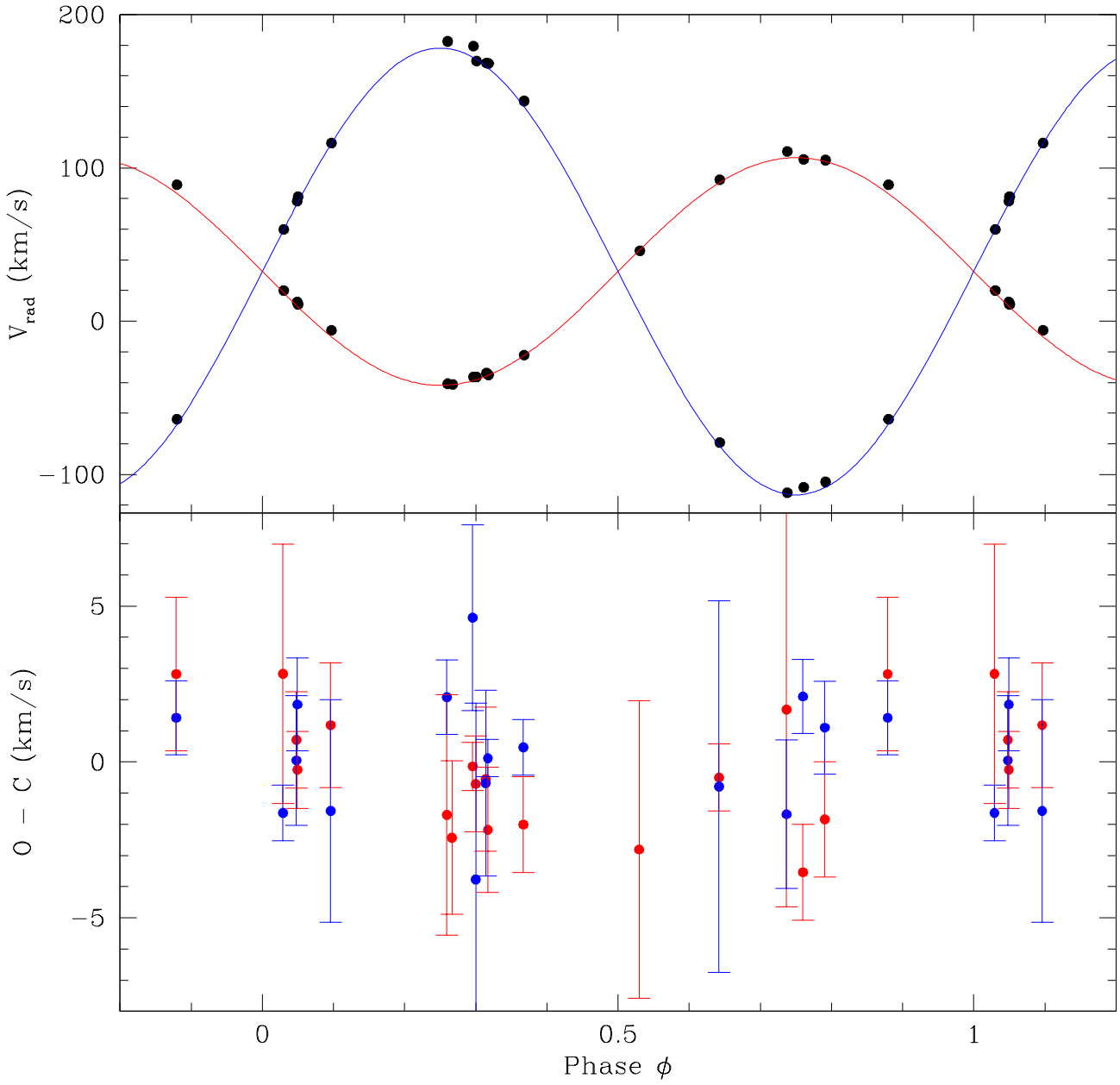


Fig. 4.— Radial velocities for KV29 phased to the binary orbit. The colored lines are the best fitting models. The bottom plot is an O-C graph with error bars scaled to give a reduced $\chi^2 \approx 1$.

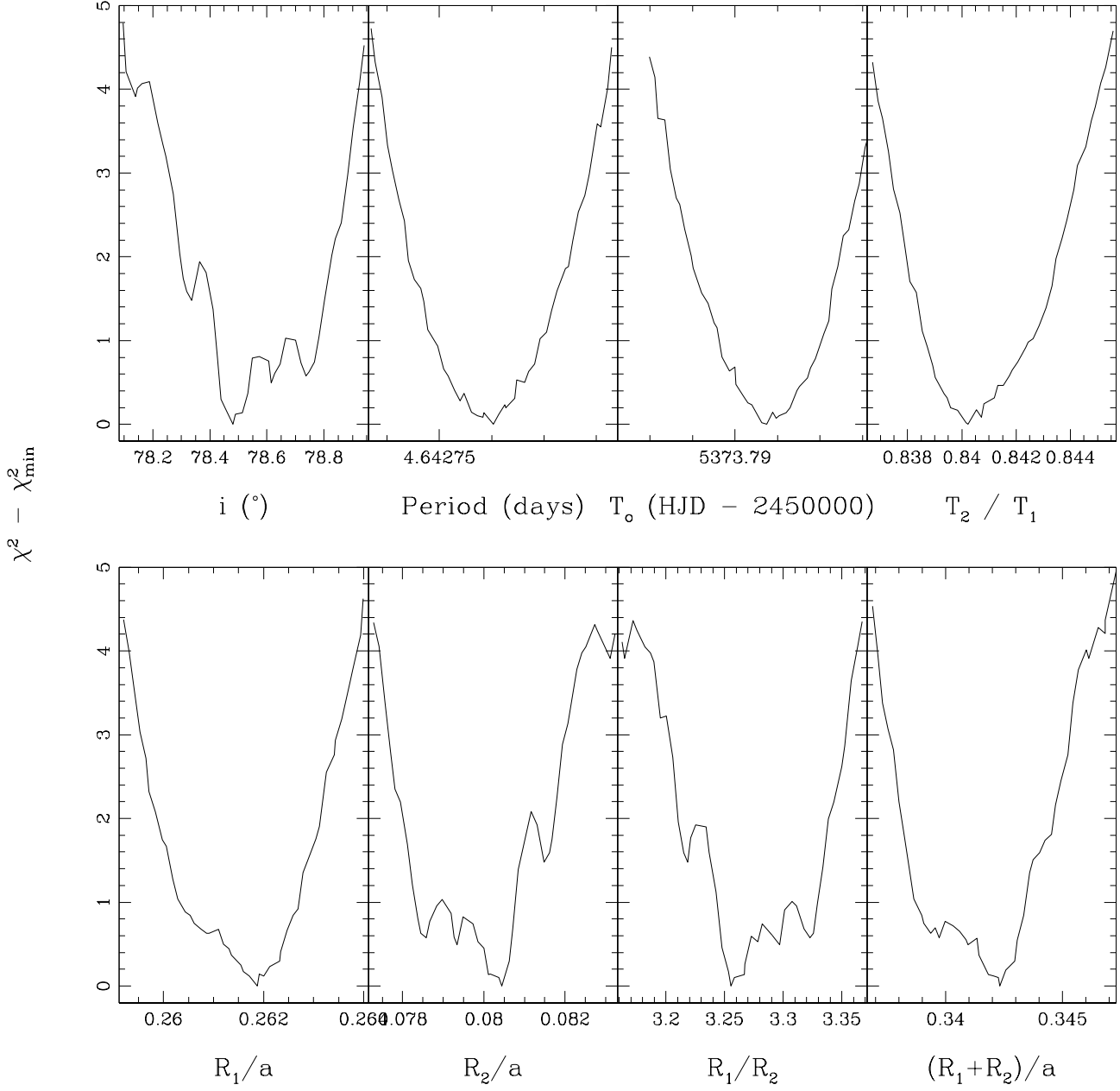


Fig. 5.— $\chi^2 - \chi_{min}^2$ plot for each of the six parameters in the constant limb darkening run.

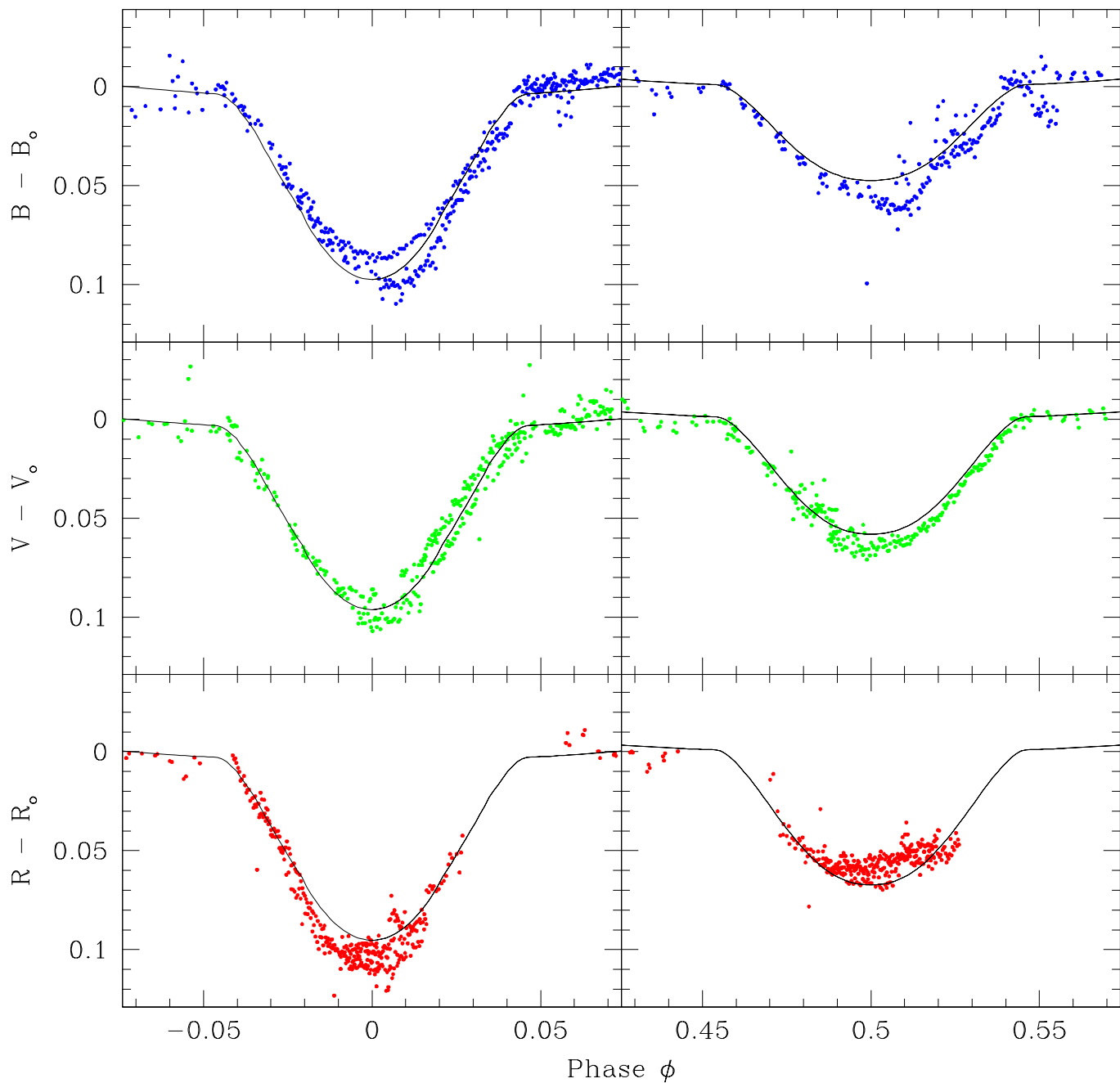


Fig. 6.— Zoom on the eclipses in BVR_c . The solid lines are the best fitting model derived from the constant limb darkening run. The median magnitude for each color has been subtracted off.

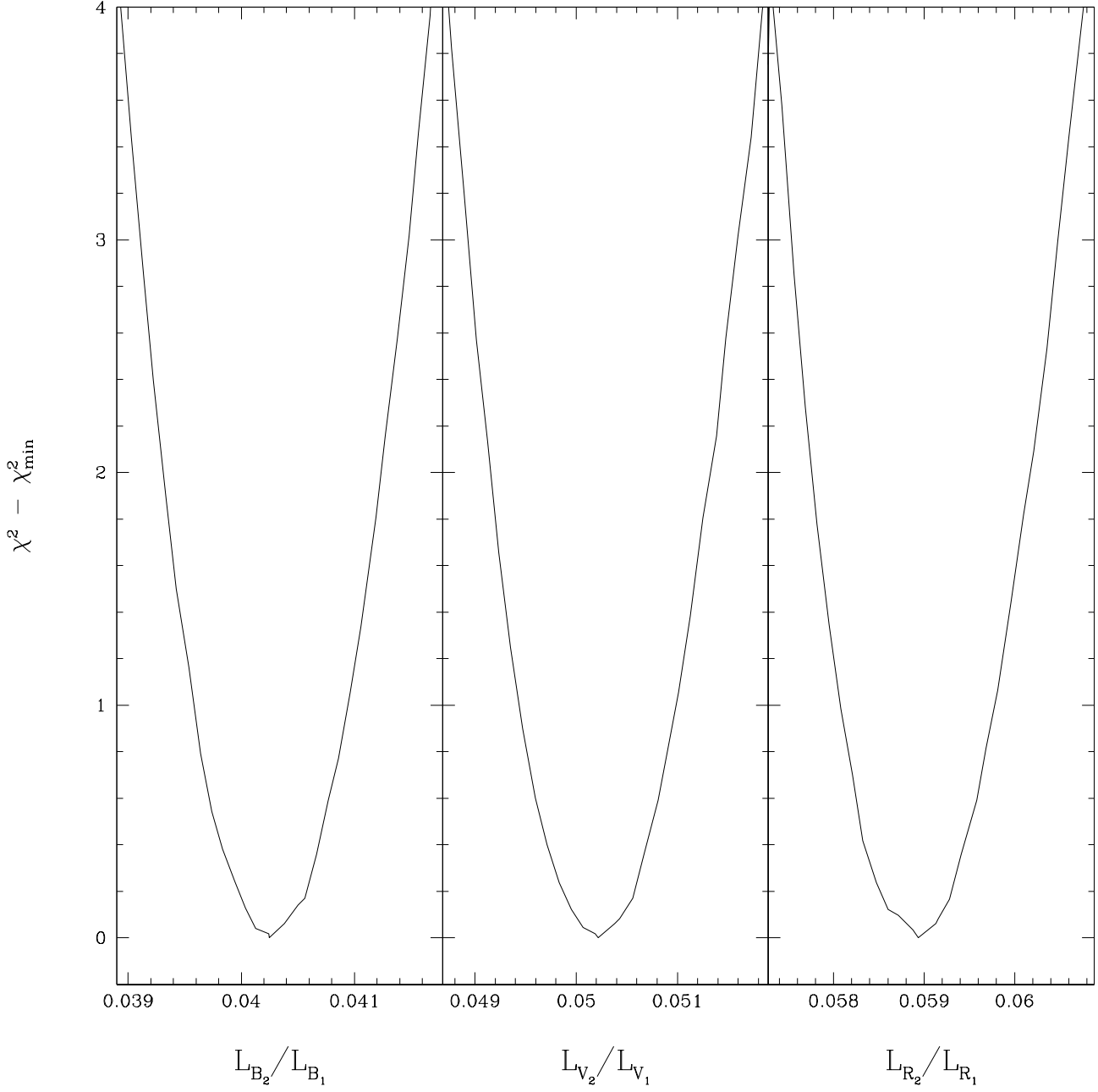


Fig. 7.— $\chi^2 - \chi_{min}^2$ plot for the luminosity ratios (L_2/L_1) in *BVR*.

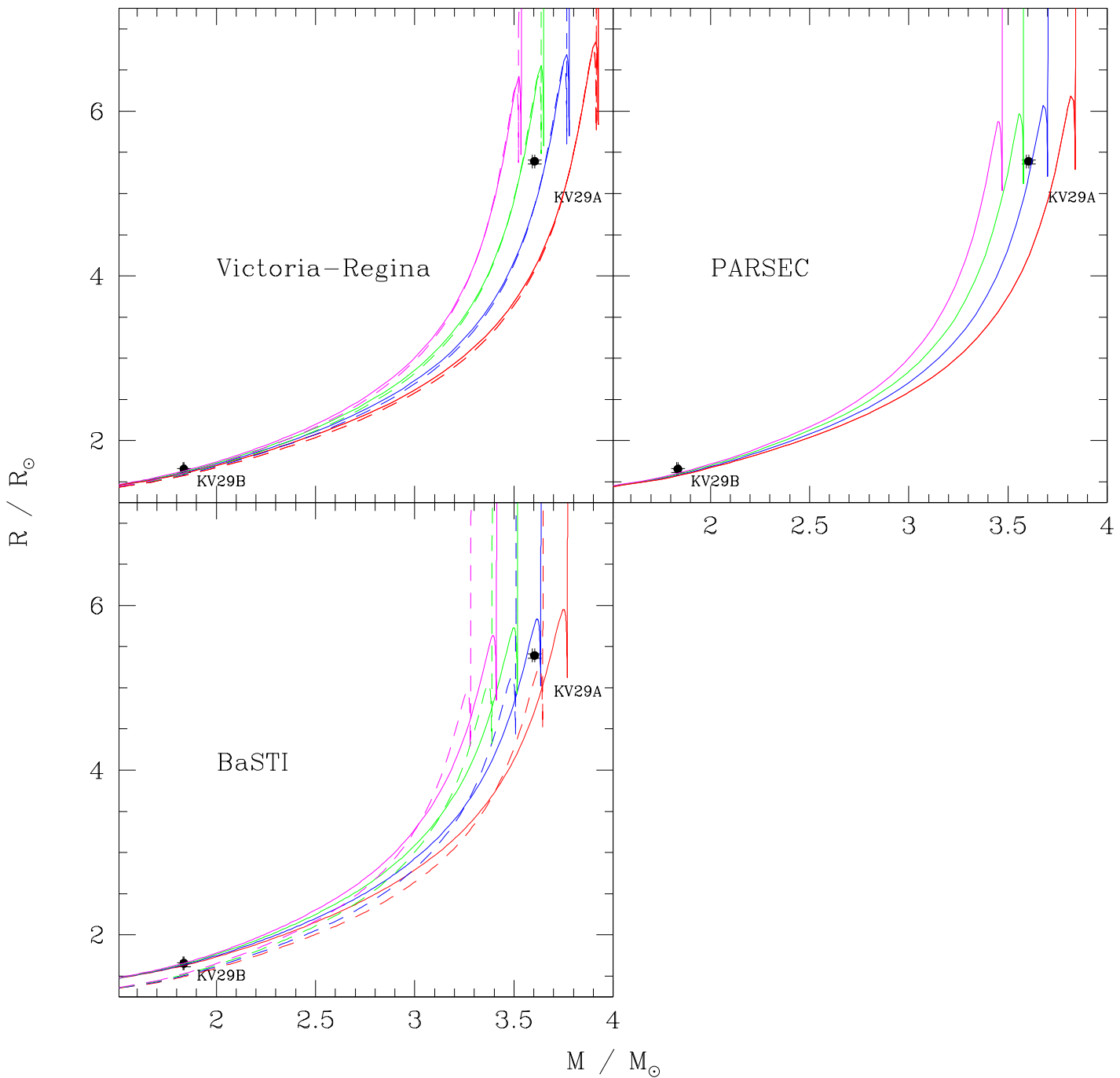


Fig. 8.— Mass-radius plots for the components of KV29. Models have ages 200 (red), 220 (blue), 240 (green), and 260 Myr (magenta). The PARSEC isochrones employ $Z = 0.0161$. The Victoria-Regina isochrones use $Z = 0.0146$ (dashed) and $Z = 0.0170$ (solid), and the BaSTI isochrones use $Z = 0.01$ (dashed) and $Z = 0.0198$ (solid) to bracket $Z = 0.0161$.

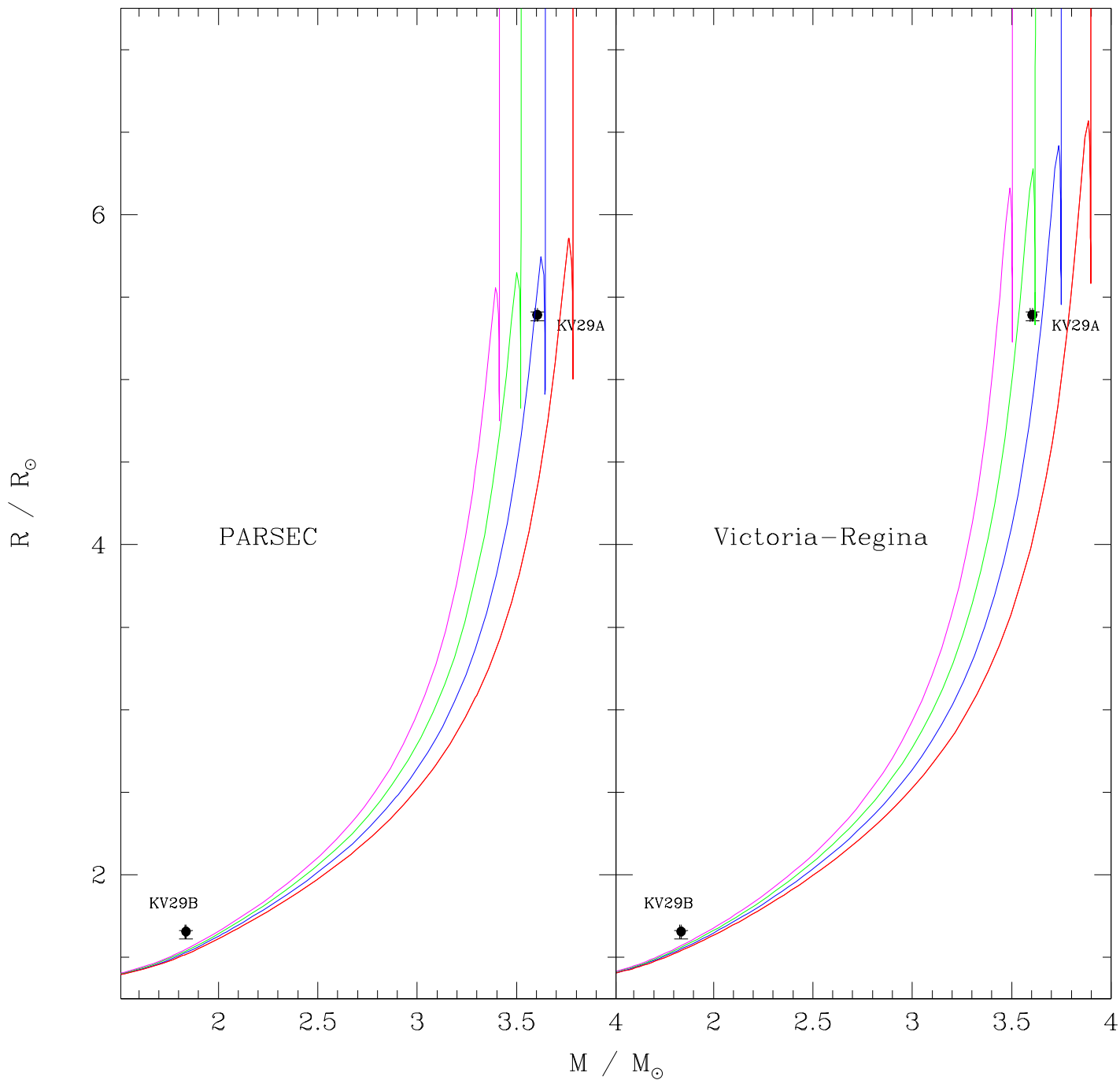


Fig. 9.— Same as mass-radius plots from Fig.8, but with $Z \approx 0.0117$ to model the lower cluster metallicity of Beaver et al. (2014). The PARSEC and Victoria-Regina isochrones used $Z = 0.0117$ and 0.0120 respectively.

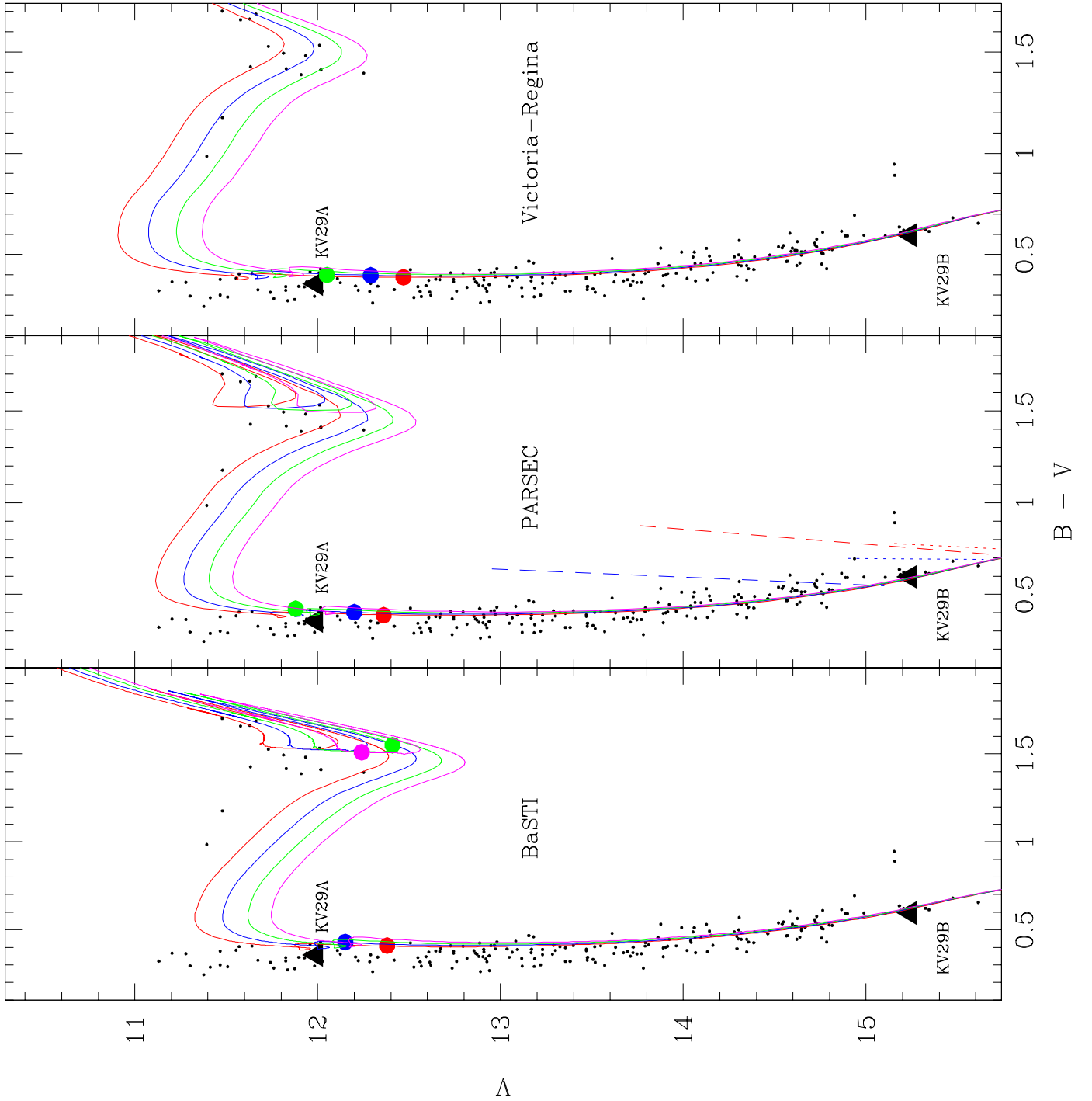


Fig. 10.— Color-magnitude diagrams for M11 (photometry from Stetson 2000). The photometry of the system and of each component are shown with triangles. Models have ages 200 (red), 220 (blue), 240 (green), and 260 Myr (magenta), and have been shifted so that the isochrones match the secondary star photometry at its measured mass. The corresponding mass of the isochrone to the primary star is shown as a large circle of the same color as the isochrone. The BaSTI, PARSEC, and Victoria-Regina isochrones use $Z = 0.0198$, 0.0161 , and 0.0146 respectively. δ Sct (long dashed) and γ Dor (short dashed) instability strips (Uytterhoeven et al. 2011) are shown in the central panel.

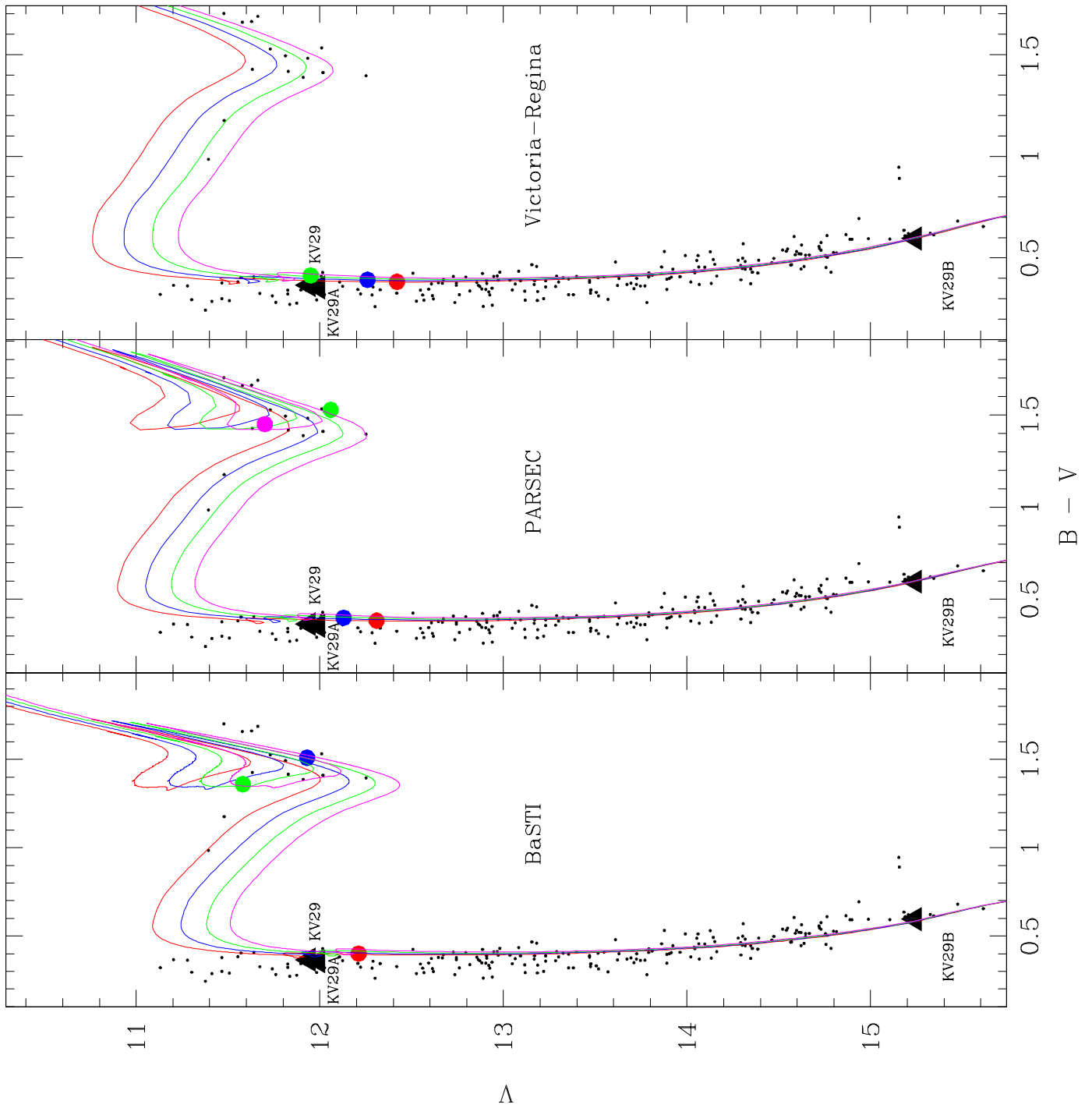


Fig. 11.— Same as Fig.10 except with the $Z \approx 0.0117$ (Beaver et al. 2014). The BaSTI, PARSEC, and Victoria-Regina isochrones use $Z = 0.01, 0.0117,$ and $0.0120,$ respectively.

Table 1. Log of Photometric Observations and Data Points

Civil Date	HJD–2450000	N_B	N_V	N_R
28 June 2009	5011		131	
29 June 2009	5012		83	
30 June 2009	5013		48	
1 June 2010	5349		111	
2 June 2010	5350	114		
10 June 2010	5358		111	
17 June 2010	5365		124	
25 June 2010	5373		21	
2 July 2010	5380		146	
9 July 2010	5387		104	
16 July 2010	5394	130		
23 July 2010	5401	133		
30 July 2010	5408	22		
1 August 2010	5410	42	45	
8 August 2010	5417	52	52	
15 August 2010	5424	41	42	
18 August 2010	5427			27
1 September 2010	5441	24	24	
6 September 2010	5446	23	23	
7 September 2010	5447	21		20
10 September 2010	5450	14	15	
14 September 2010	5454	21	21	19
17 September 2010	5457	17	17	17
19 September 2010	5459			82
21 September 2010	5461	11	14	15
26 September 2010	5466			74
27 May 2011	5709		60	
22 June 2011	5735			150
29 June 2011	5742			79
6 July 2011	5749			151
13 July 2011	5756			147
20 July 2011	5763	83		
7 August 2011	5781	40		
13 August 2011	5787	37	36	34
18 August 2011	5792	25		26
27 May 2013	6439			59

Table 2. HET Spectroscopic Observations

UT Date	HJD–2450000	Phase	V_1 (km s ⁻¹) ^a	V_2 (km s ⁻¹) ^a
6 May 2010	5322.9402	0.049	12.39 ± 1.54	78.29 ± 2.08
6 May 2010	5322.9461	0.050	11.09 ± 1.23	81.19 ± 1.49
15 June 2010	5362.8405	0.643	92.27 ± 1.08	-79.13 ± 5.96
25 June 2010	5372.8164	0.792	105.03 ± 1.85	-104.92 ± 1.49
28 July 2010	5405.7272	0.880	89.00 ± 2.47	-64.00 ± 1.19
1 August 2010	5409.7096	0.738	110.68 ± 6.32	-111.87 ± 2.38
13 August 2010	5421.6892	0.318	-34.97 ± 2.00	168.13 ± 0.60
5 September 2010	5444.6364	0.261	-40.83 ± 3.85	182.52 ± 1.19
12 September 2010	5451.6024	0.761	105.58 ± 1.54	-108.32 ± 1.19
19 September 2010	5458.5978	0.268	-41.29 ± 2.47	-
24 August 2011	5797.6628	0.297	-36.37 ± 0.77	179.38 ± 2.98
29 August 2011	5802.6365	0.368	-22.13 ± 1.54	143.62 ± 0.89
7 September 2011	5811.6120	0.301	-36.32 ± 1.54	169.78 ± 5.66
20 September 2011	5824.5937	0.097	-5.97 ± 2.00	116.13 ± 3.57
21 September 2011	5825.6048	0.315	-33.89 ± 2.31	168.41 ± 2.98
22 September 2011	5826.6063	0.531	45.96 ± 4.78	-
29 September 2011	5833.5679	0.030	20.07 ± 4.16	59.82 ± 0.89

^aErrors are scaled to return a reduced $\chi^2 \approx 1$

Table 3. Constrained Values for KV29

Parameter	Value
$Q = M_2/M_1$	0.509 ± 0.004
K_p (km s ⁻¹)	74.25 ± 0.50
e	0.0
T_1 (K)	9480 ± 550
γ (km s ⁻¹)	32.39 ± 1.90
$x_{R,1}$	0.2710
$y_{R,1}$	0.4228
$x_{R,2}$	0.3504
$y_{R,2}$	0.3981
$x_{V,1}$	0.2159
$y_{V,1}$	0.3824
$x_{V,2}$	0.2765
$y_{V,2}$	0.3764
$x_{B,1}$	0.1634
$y_{B,1}$	0.3416
$x_{B,2}$	0.1947
$y_{B,2}$	0.1241

Table 4. Best-Fit Model Parameters for KV29

Parameter	Constant LD ^a	Fitted LD ^b
i ($^\circ$)	$78.48^{+0.30}_{-0.06}$	$78.38^{+0.37}_{-0.25}$
P (d)	4.64276 ± 0.00001	4.64287 ± 0.00006
t_o (HJD)	2455373.788 ± 0.001	2455373.790 ± 0.001
R_1/a	$0.2620^{+0.0008}_{-0.0014}$	0.267 ± 0.002
R_2/a	$0.0804^{+0.0003}_{-0.0021}$	0.078 ± 0.002
R_1/R_2	$3.256^{+0.074}_{-0.011}$	$3.428^{+0.089}_{-0.067}$
$(R_1 + R_2)/a$	$0.342^{+0.001}_{-0.003}$	$0.345^{+0.003}_{-0.004}$
T_2/T_1	0.840 ± 0.002	0.866 ± 0.005
a/R_\odot	$20.591^{+0.004}_{-0.022}$	$20.608^{+0.017}_{-0.007}$
$a \sin i/R_\odot$	20.176 ± 0.021	20.17652 ± 0.00006
M_1/M_\odot	$3.604^{+0.002}_{-0.011}$	$3.613^{+0.009}_{-0.004}$
M_2/M_\odot	$1.837^{+0.001}_{-0.006}$	$1.842^{+0.005}_{-0.002}$
R_1/R_\odot	$5.392^{+0.018}_{-0.035}$	$5.407^{+0.001}_{-0.040}$
R_2/R_\odot	$1.656^{+0.007}_{-0.044}$	$1.699^{+0.052}_{-0.001}$
$\log g_1$ (cgs)	$3.531^{+0.004}_{-0.003}$	$3.530^{+0.006}_{-0.0}$
$\log g_2$ (cgs)	$4.264^{+0.022}_{-0.004}$	$4.243^{+0.0}_{-0.025}$
$M_1 \sin^3 i$ (M_\odot)	3.391 ± 0.011	3.391 ± 0.003
$M_2 \sin^3 i$ (M_\odot)	1.728 ± 0.005	1.7283 ± 0.0005
$V_{1,rot} \sin i$ (km s $^{-1}$) ^c	$57.60^{+0.18}_{-0.32}$	$58.30^{+0.35}_{-0.46}$
$V_{2,rot} \sin i$ (km s $^{-1}$) ^c	$17.69^{+0.07}_{-0.46}$	$17.01^{+0.39}_{-0.52}$

^aUsed all photometry. Preferred fit.

^bUsed phase-binned light curves.

^cCalculated assuming synchronous rotation.

Table 5. Deconvolved Photometry of KV29

Name	V	$B - V$
KV29	11.921 ± 0.004^a	0.392 ± 0.008^a
KV29A	11.974 ± 0.005	0.382 ± 0.008
KV29B	15.226 ± 0.015	0.624 ± 0.023

^aStetson (2000)